ADVANCED MATERIALS
www.advmat.de

Reinforcing the Electrode/Electrolyte Interphases of Lithium Metal Batteries Employing Locally Concentrated Ionic Liquid Electrolytes

*Xu Liu, Alessandro Mariani, Thomas Diemant, Maria Enrica Di Pietro, Xu Dong, Andrea Mele, and Stefano Passerini**

Lithium metal batteries (LMBs) with nickel-rich cathodes are promising candidates for next-generation high-energy-density batteries, but the lack of sufficiently protective electrode/electrolyte interphases (EEIs) limits their cyclability. Herein, trifluoromethoxybenzene is proposed as a cosolvent for locally concentrated ionic liquid electrolytes (LCILEs) to reinforce the EEIs. With a comparative study of a neat ionic liquid electrolyte (ILE) and three LCILEs employing fluorobenzene, trifluoromethylbenzene, or trifluoromethoxybenzene as cosolvents, it is revealed that the fluorinated groups tethered to the benzene ring of the cosolvents not only affect the electrolytes' ionic conductivity and fluidity, but also the EEIs' composition via adjusting the contribution of the 1-ethyl-3-methylimidazolium cation ($Emim^+$) and bis(fluorosulfonyl)imide anion. Trifluoromethoxybenzene, as the optimal cosolvent, leads to a stable cycling of LMBs employing 5 mAh cm^{-2} lithium metal anodes (LMAs), 21 mg cm^{-2} $LiNi_{0.8}Co_{0.15}Al_{0.05}$ (NCA) cathodes, and 4.2 µL mAh^{-1} electrolytes for 150 cycles with a remarkable capacity retention of 71%, thanks to a solid electrolyte interphase rich in inorganic species on LMAs and, particularly, a uniform cathode/electrolyte interphase rich in $Emim^+$-derived species on NCA cathodes. By contrast, the capacity retention under the same condition is only 16%, 46%, and 18% for the neat ILE and the LCILEs based on fluorobenzene and benzotrifluoride, respectively.

1. Introduction

Lithium metal batteries (LMBs) pairing high-energy lithium metal anodes (LMAs) and nickel-rich cathodes, e.g., $LiNi_{0.8}Mn_{0.1}Co_{0.1}O_2$ (NMC811) and $LiNi_{0.8}Co_{0.15}Al_{0.05}O_2$ (NCA), are promising candidates of the next-generation secondary batteries.[1,2] However, these highly active electrode materials usually exhibit poor interfacial compatibility with conventional electrolytes due to the lack of sufficiently protective electrolyte/electrode interphases (EEIs), leading to severe side reactions at the interface and a series of issues negatively affecting the cyclability, e.g., dendritic lithium growth, low Coulombic efficiency (CE), material passivation, and electrolyte depletion.[3,4] In fact, practical LMBs targeting high energy density require high-loading cathodes (typical industry level is 3.5 mAh cm^{-2}), low negative to positive areal capacity (N/P) ratios, and lean electrolytes (typical industry level for electrolyte to capacity (E/C) ratios is ≈2–5 g $(Ah)^{-1}$),[5] which frequently result in capacity fading due to the interfacial side reactions.[6,7] Electrolytes play a key role in the formation of the EEIs, yielding interfacial stability, and their composition optimization has been demonstrated as an effective strategy in achieving high interfacial stability and long life span of LMBs.[8–11]

Low-flammability ionic liquid electrolytes (ILEs) with high compatibility toward LMAs and Ni-rich cathodes are

X. Liu, T. Diemant, X. Dong, S. Passerini
Helmholtz Institute Ulm (HIU)
Helmholtzstraße 11, D-89081 Ulm, Germany
E-mail: stefano.passerini@kit.edu
X. Liu, T. Diemant, X. Dong, S. Passerini
Department of Chemistry and Biosciences
Karlsruhe Institute of Technology (KIT)
P.O. Box 3640, D-76021 Karlsruhe, Germany
The ORCID identification number(s) for the author(s) of this article can be found under https://doi.org/10.1002/adma.202309062

DOI: 10.1002/adma.202309062

A. Mariani
ELETTRA Sincrotrone Trieste
Basovizza, Trieste I-34012, Italy
M. E. Di Pietro, A. Mele
Department of Chemistry
Materials and Chemical Engineering "Giulio Natta"
Politecnico di Milano
Piazza Leonardo da Vinci 32, Milan I-20133, Italy
S. Passerini
Chemistry Department
Sapienza University of Rome
Piazzale Aldo Moro 5, Rome I-00185, Italy

promising candidates.[12–15] Particularly, the recently developed locally concentrated ionic liquid electrolytes (LCILEs), i.e., mixtures of nonsolvating cosolvents and concentrated ILEs, effectively mitigate neat ILEs' drawbacks of high viscosity and sluggish ion transport at room temperature, enabling the use of high mass-loading cathodes, e.g., 10 mg cm^{-2}, and current densities up to 2 mA cm^{-2}.[16–18] The addition of the cosolvent, which is less expensive than the ionic liquid, also reduces the cost of the electrolyte. Furthermore, previous investigations have revealed a dramatic influence of the cosolvent on the EEIs as well as the interfacial stability.[19–21] For instance, the lithium stripping/plating CE is only 98.22% in a neat ILE consisting of lithium bis(fluorosulfonyl)imide (LiFSI) and 1-ethyl-3-methylimidazolium bis(fluorosulfonyl)imide (EmimFSI) in a molar ratio of 1:2, i.e., $[LiFSI]_1[EmimFSI]_2$ (FE), while this value is improved to 99.20% and 99.57% as a consequence of the formation of more protective solid electrolyte interphases (SEIs) when bis(2,2,2-trifluoroethyl) and 1,2-difluorobenzene are employed as cosolvents, respectively.[22,23] Moreover, the incorporation of 1,2-difluorobenzene into FE significantly mitigates the thickening of cathode/electrolyte interphases (CEIs) in FE, which effectively promotes the reversibility and cyclability of NMC811 cathodes.[23] Therefore, the optimization of the cosolvent of LCILEs is worth being further explored for more practical LMBs.

Fluorinated aromatic compounds are a new class of diluents for concentrated electrolytes with respect to the more classic fluorinated ethers. The earliest fluorinated aromatic diluents are 1,2-difluorobenzene and monofluorobenzene (BnF) reported by Yoo et al. and Jiang et al. in 2021, respectively.[24,25] With lower cost, lower density, and stronger F-donating ability, these two aromatic cosolvents are demonstrated as better choice than fluorinated ethers for ether-, carbonate-, phosphate-, and ionic-liquid-based concentrated electrolytes.[24–27] Meanwhile, some other fluorinated aromatic diluents with more fluorine atoms on the benzene ring or different fluorinated groups have been proposed, e.g., 1,3,5-trifluorobenzene, trifluoromethylbenzene (BnCF), and trifluoromethoxybenzene (BnOCF).[28–30] It is also demonstrated that, for a glyme-based concentrated electrolyte, BnCF and BnOCF as cosolvents could participate in the formation of more protective EEIs through a milder and more controllable defluorination process in comparison to 1,2-difluorobenzene.[30] To the best of our knowledge, LCILEs based on BnCF or BnOCF have not been explored yet, and the effect of these different fluorinated groups attached to the benzene ring on the physical properties and electrochemical behaviors of LCILEs remains unknown.

Herein, a systematic comparative study of three LCILEs employing BnF, BnCF, or BnOCF as the cosolvent and the neat ILE, i.e., FE, is conducted in terms of physical properties, solution structure, electrochemical performance, as well as EEIs on both LMAs and NCA cathodes. The results demonstrate that the fluorinated groups tethered to the benzene ring of the cosolvents not only affect the electrolytes' ionic conductivity and fluidity, but also the EEIs' composition via adjusting the contribution of $Emim^+$ and FSI^-. Among the cosolvents, BnOCF is verified as the optimal one leading to a remarkably stable cycling of Li/NCA cells with a cathode areal capacity of 4.2 mAh cm^{-2}, a N/P ratio of 1.2, and an E/C ratio of 4.2 μL mAh^{-1} for 150 cycles with a capacity retention of 71%, thanks to the generation of a thin but protective SEI on LMAs and, particularly, a uniform CEI rich in $Emim^+$-derived compounds on the NCA cathodes. By contrast, the capacity retention of the Li/NCA cells employing FE and LCILEs based on BnF and BnCF is only 16%, 46%, and 18%, respectively, under the same conditions.

2. Results and Discussion

2.1. Physical Properties and Solvation Structure

The BnF-, BnCF-, and BnOCF-based LCILEs are named in the following FEF, FECF, and FEOCF, respectively; their composition can be described as $[LiFSI]_1[EmimFSI]_2[X]_{0.55}$ (X = BnF, BnCF, or BnOCF), i.e., LiFSI, EmimFSI, and cosolvent X are in a molar ratio of 1:2:0.55. $Emim^+$ was selected as the IL's cation because of its conjugated structure and high nitrogen content. The former helps delocalizing the positive charge, further weakening the interaction with FSI^-, i.e., lowering the viscosity thus enhancing Li^+ transport. The latter is beneficial to the formation of a more protective, nitrogen-rich SEI on LMAs.[22] Sketches of the chemical structures of the electrolyte components are shown in Figure S1 (Supporting Information).

Figure 1a,b shows the ionic conductivity and viscosity of the electrolytes at various temperatures from 10 to 40 °C. The specific values can be found in Tables S1 and S2 (Supporting Information). In general, the addition of the cosolvents led to promoted ion transport and fluidity, while the promotional effect of the cosolvents followed the trend of BnF > BnOCF > BnCF. Specifically, at 20 °C, the ionic conductivity of FE, FEF, FECF, and FEOCF was 5.28, 6.80, 6.10, and 6.38 mS cm^{-1}, respectively, while the corresponding viscosity was 67, 44, 49, and 46 mPa s, respectively. The self-diffusion coefficient of the species in the electrolytes at 293 K was measured via pulsed field gradient NMR. The obtained values for the Li^+, FSI^-, and $Emim^+$ ions are shown in Figure 1c. The diffusion coefficient of ions (D) is inversely proportional to the macroscopic viscosity (η) of the liquid and the hydrodynamic radius of the ions (r), according to the Stokes–Einstein equation[31]

$$D = \frac{k_B T}{6\pi\eta r} \quad (1)$$

where k_B is the Boltzmann constant and T is the temperature. For FE, FECF, and FEOCF, the self-diffusion coefficient of the ions followed the trend FEOCF > FECF > FE, well correlating with the promotional effect of the cosolvents on the fluidity of the electrolytes. However, the ions in FEF exhibited equal (i.e., Li^+ and FSI^-) and even lower (i.e., $Emim^+$) self-diffusion coefficient with respect to that in FEOCF, despite a lower viscosity of FEF than FEOCF. This phenomenon supports for different hydrodynamic radii of the ions and is symptomatic of their different coordination environments in the various electrolytes. In general, these results demonstrate the influence of the different fluorinated groups of the benzene-based cosolvents on the physical properties of the LCILEs, and imply different effects on the ion–ion and/or ion–solvent interactions.

The solvation of Li^+ is relevant to both the Li^+ transport in the bulk electrolyte and the de-/solvation of Li^+ at the electrode/electrolyte interfaces, affecting the electrochemical

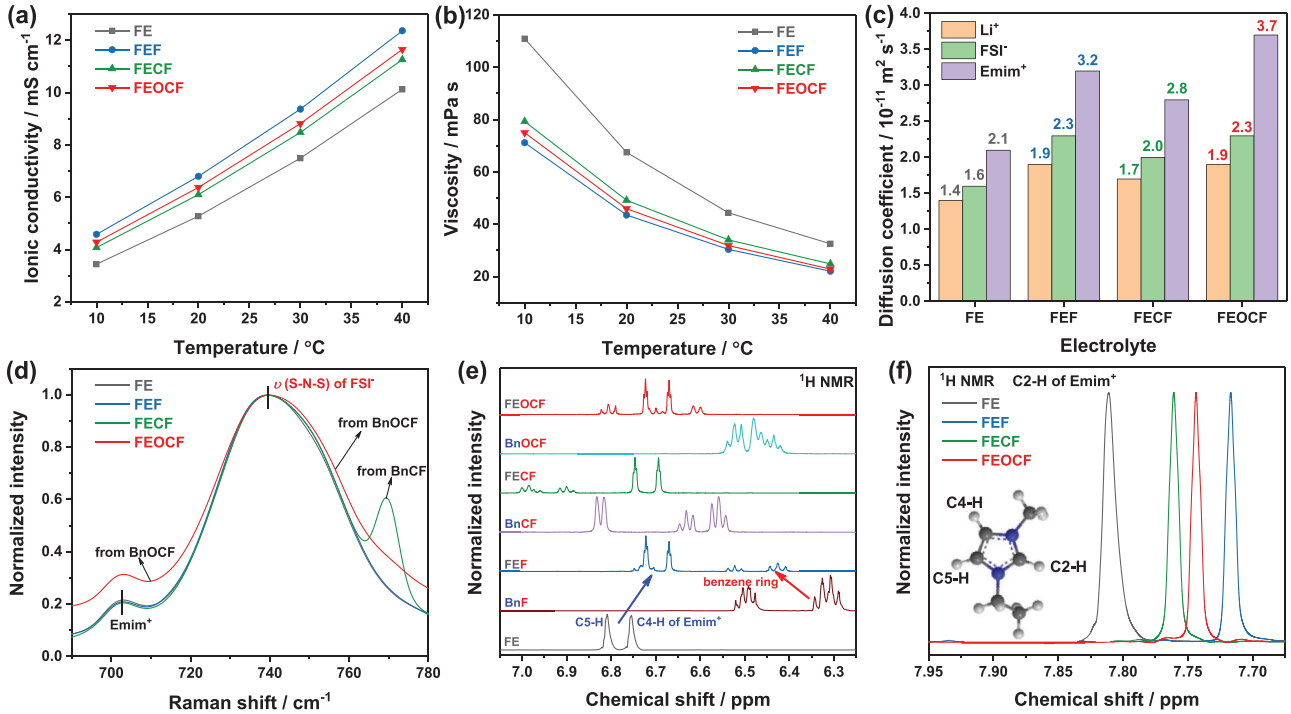

Figure 1. a) Viscosity, b) ionic conductivity, c) ion self-diffusion coefficients via NMR, and d) FSI^--related Raman peak of the electrolytes. 1D ^{1}H NMR spectra of the electrolytes and their constituents in the region of e) 6.25–7.05 ppm and f) 7.675–7.950 ppm. The inset of (f) shows a sketch of the chemical structure of $Emim^+$ with the C2—H, C4—H, and C5—H marked.

performance of the batteries.[32–34] To characterize the coordination of Li^+, Raman spectra of FE and the three LCILEs were recorded. The Raman spectra in the region of 680–780 cm^{-1}, where the characteristic ν_s(S—N—S) mode of FSI^- occurs, were first checked.[35] The normalized spectra are shown in Figure 1d, while the original spectra of the electrolytes and the neat components, i.e., EmimFSI and the cosolvents, are shown in Figures S2 and S3 (Supporting Information), respectively. For the neat EmimFSI (Figure S3a, Supporting Information), the main peak located at 725 cm^{-1} originates from the "free" FSI^- weakly coordinating to the bulky, charge-delocalized $Emim^+$, and it was accompanied by a minor peak resulting from $Emim^+$ around 705 cm^{-1}.[35,36] In case of FE, the main peak was upshifted to 739 cm^{-1} due to the coordination between FSI^- and Li^+.[36] Upon addition of the cosolvents to FE, the main peak does not show obvious shift, demonstrating that the cosolvents do not significantly affect the coordination between Li^+ and FSI^-. It is also noticed that the edge of the FSI^- peak overlaps with peaks from the cosolvents which appears in the regions of 680–710 and 750–780 cm^{-1}, as shown in Figure S3b–d (Supporting Information). Due to the presence of these peaks, a detailed fitting analysis of the coordination state of FSI^- in the electrolytes is not feasible. The similar situation occurs for the FSI^- ν(O=S=O) mode in the region of 1200–1250 cm^{-1}, as displayed in Figure S4 (Supporting Information).[35]

The focus was then shifted to the interaction between $Emim^+$ and cosolvents, which was characterized via ^{1}H NMR spectroscopy.[37,38] Figure 1e shows the ^{1}H NMR spectra of the electrolytes and the cosolvents. For the neat ILE, peaks at 6.82 and 6.76 ppm are assigned, respectively, to the C5—H and C4—H of $Emim^+$, as illustrated in the inset of Figure 1f.[39] For the neat cosolvents, peaks from the protons of their benzene ring were observed, i.e., 6.25–6.55 ppm for BnF, 6.5–6.85 ppm for BnCF, and 6.4–6.60 ppm for BnOCF. When the cosolvents and FE were mixed, the peaks from $Emim^+$ shifted to lower frequencies (upfield shift) and the peaks from the cosolvents shifted to higher frequencies (downfield shift). A similar development was previously reported for LCILEs based on $Emim^+$ and 1,2-diflurobenzene, for which it was demonstrated that the shifts result from the charge transfer from $Emim^+$ to 1,2-diflurobenzene via their π–π stacking.[23] Correspondingly, the observed shift in this work indicates the establishment of π–π interactions between $Emim^+$ and the fluorinated aromatic cosolvents. An upfield shift was also observed for C2—H peak of $Emim^+$ (see Figure 1f), and it followed the trend of FEF > FEOCF > FECF. This trend is identical to the promotion of the electrolytes' ionic conductivity and fluidity by the cosolvents, implying a correlation between them.

To decipher the ion–ion and ion–cosolvent interactions in the LCILEs, molecular dynamics (MD) simulations of the three LCILEs were conducted. The snapshots of the simulation box are shown in **Figure 2**a–c where the semitransparent blue clouds, yellow spheres, and red beads represent $Emim^+$/FSI^-, Li^+, and cosolvents, respectively. In general, the three systems are quite similar. Li^+, $Emim^+$, and FSI^- generate a continuous matrix in which the cosolvents are embedded. Importantly, the red beads tend to cluster together leading to an inhomogeneous distribution in the simulation boxes, which hints at a poor affinity of the cosolvents toward ions.

The solvation of Li^+ in the simulated electrolytes was characterized via radial distribution functions (RDFs). The Li—O(FSI),

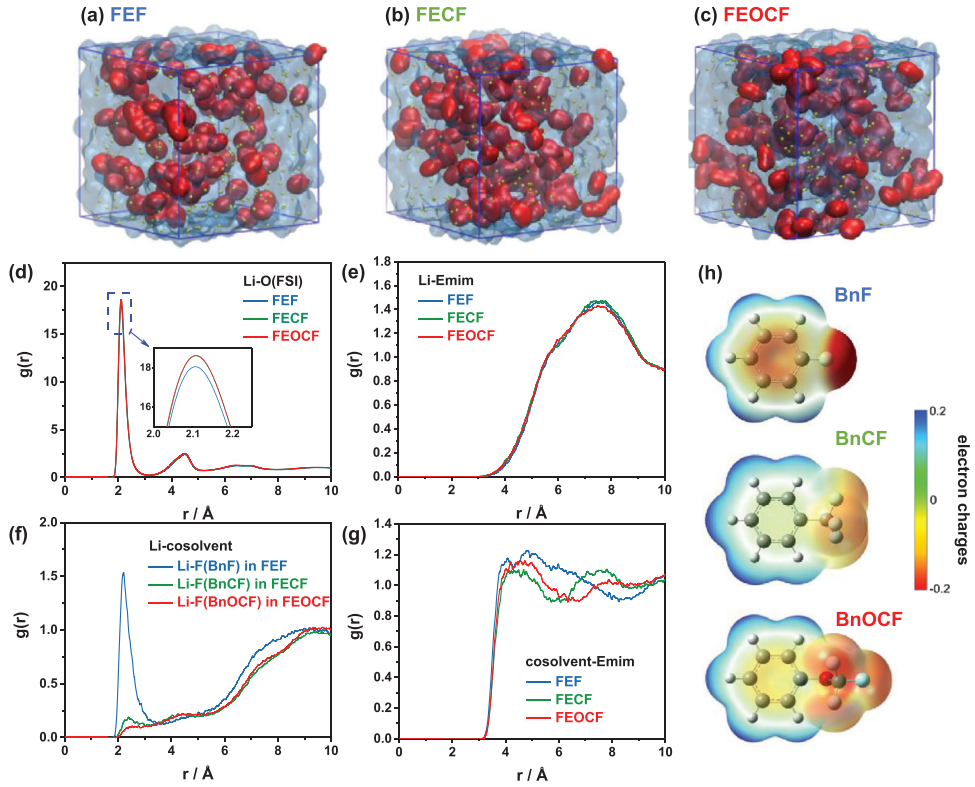

Figure 2. Results of MD simulations for FEF, FECF, and FEOCF electrolytes: Snapshots of the simulation box of a) FEF, b) FECF, and c) FEOCF; radial distribution functions of d) Li—O(FSI), e) Li—Emim, f) Li—F(cosolvent), and g) cosolvent—Emim in the LCILEs. h) Calculated electrostatic surface potentials for BnF, BnCF, and BnOCF via DFT simulations.

Li—Emim, and Li—F(cosolvent) curves are shown in Figure 2d–f, representing the coordination of Li^+ by the oxygen from FSI^-, the geometric center of the $Emim^+$ ring (the middle point of the 5-member ring), and the fluorine of cosolvents, respectively. In general, the Li—O(FSI) and Li—Emim profiles of the three LCILEs are very similar. As expected, Li^+ coordinates in the aforementioned ion matrix preferentially to FSI^- rather than $Emim^+$, leading to a sharp maximum in the Li—O(FSI) curves at 2.1 Å and negligible intensity in the region below 3.0 Å in the Li—Emim curves. The interaction between $Emim^+$ and FSI^- in the electrolytes was also compared, but does not show any difference, as displayed in Figure S5a (Supporting Information). On the contrary, the Li—F(cosolvent) curves for the three systems are rather different. The interaction is fairly structured for BnF, as evidenced by a peak at 2.2 Å, which is almost completely absent in the other two systems. In fact, the presence of BnF in the first solvation shell of Li^+ substitutes a few FSI^-, which is evidenced by a slightly lower intensity of the peak located at 2.1 Å in the Li—O(FSI) curve for FEF with respect to the other two electrolytes (see inset of Figure 2d). The occurrence of this substitution is expected leading to lower viscosity and higher ionic conductivity. On the other hand, the stronger interaction between Li and BnF compared to BnOCF is a factor contributing to slowing down the lithium diffusivity in FEF with respect to FEOCF. The Li^+ diffusion coefficients reported in Figure 1c follow the trend of FEF ≈ FEOCF, which is different from that predicted solely based on fluidity (FEF > FEOCF). It needs to be stressed that the reduced peak intensity is not significant, due to the low content of BnF in FEF and less preferred coordination of Li^+ to BnF with respect to FSI^-. Therefore, the revealed solvation of Li^+ is generally identical to the results of Raman spectra.

The solvation of the cosolvents was also checked. Figure S6 (Supporting Information) shows the RDF profiles of cosolvent—$Emim^+$, cosolvent–cosolvent, and cosolvent—O(FSI) in the simulated electrolytes. The first solvation sheath of the cosolvents at a distance of around 4 Å is mainly occupied by cosolvents and $Emim^+$. Figure 2g and Figure S7 (Supporting Information) compare the cosolvent—Emim and cosolvent–cosolvent RDF profiles in the LCILEs, respectively. These two pairs both governed by π–π interactions are in a competition in the first solvation shell of the cosolvent, as the intensity of cosolvent—$Emim^+$ curves around 4 Å follows the trend of FEF > FEOCF > FECF and that of cosolvent–cosolvent curves follows the trend of FEF < FEOCF < FECF. The simulated results are consistent to the observed shift of $Emim^+$ peaks in the ^{1}H NMR spectra shown in Figure 1e,f. One can further infer that a cosolvent preferring to interact with $Emim^+$ rather than cosolvent itself can more effectively promote the fluidity and ion transport of the electrolytes. Additionally, at the molecular level, the more efficient π–π interactions experienced by $Emim^+$ in FEF with respect to FEOCF is expected leading to a larger hydrodynamic radius, which translates into a lower $Emim^+$ diffusion coefficient in FEF despite its lower viscosity. Since FSI^- coordinates to

either Li^+ or $Emim^+$, the slowed diffusion coefficient of the cations in FEF also poses an effect on the mobility of FSI^-.

To understand the origin of the different coordination of the cosolvents' fluorine atoms toward Li^+ and the different π–π interactions between the cosolvents and $Emim^+$, the electrostatic surface potentials for the three cosolvent molecules were calculated via density functional theory (DFT) simulations and are shown in Figure 2h. Evidently, there is a much higher electron density on the fluorine atom of BnF, whereas the other two molecules appear to have a markedly less distinct charge localization on each fluorine atom. This explains the more intense interactions between Li^+ and fluorine of the cosolvent in FEF with respect to FECF and FEOCF. The negative charge on the benzene ring of the cosolvents went in the order of BnF > BnOCF > BnCF. The stronger negative charge on the benzene ring makes the cosolvent more intensively attracted by the positively charged, conjugated $Emim^+$ for π–π stacking.

2.2. Electrochemical Performance of LMAs

The electrochemical performance of LMAs in the electrolytes was investigated at 20 °C employing coin cells. The rate capability was examined with Li/Li symmetric cells. The voltage profiles of the cells during stripping/plating at different current densities from 0.1 to 2.0 mA cm^{-2} while keeping the areal capacity at 1 mAh cm^{-2} in each cycle, are shown in **Figure 3**a. The addition of cosolvents led to generally lower polarization, due to the promoted ion transport of the electrolyte. For the cells based on LCILEs with different cosolvents, the voltage plateaus at current densities lower than 0.5 mA cm^{-2} were rather similar, while clear differences appeared at elevated current rates as shown in Figure S8 (Supporting Information). For example, Figure 3b shows the average voltage plateaus of the cells at 1 mA cm^{-2}. The values for FE, FEF, FECF, and FEOCF were 83, 55, 64, and 45 mV, respectively. It is noticed that the polarization of the Li/Li cells does not correspond to the ionic conductivities of the electrolytes, which implies for a non-negligible contribution of the SEI to the cell polarization upon lithium stripping/plating.

The CE of lithium stripping/plating in the electrolytes was tested via cycling lithium metal deposited on Cu in Li/Cu cells.[30,40] The voltage evolution of the cells during the tests is summarized in Figure 3c. The CE after the initial formation cycle was measured to be 99.19% for the neat ILE. When FEF and FEOCF were employed as the electrolytes, the CE was improved to 99.57% and 99.54%, respectively, demonstrating the beneficial effect of BnF and BnOCF by reducing the interfacial side reactions and promoting the reversibility of LMAs. By contrast, a short circuit occurred to the cell with FECF electrolyte after 45 cycles with a plating current density of 0.5 mA cm^{-2}, a stripping current density of 1.5 mA cm^{-2}, and a cycling areal capacity of 1 mAh cm^{-2} for each stripping/plating cycle.

The long-term cyclability of LMAs in the electrolytes was further tested with Li/Li cells with a cycling capacity of 1 mAh cm^{-2} for each cycle. The cells were initially operated at 0.1 mA cm^{-2} for two formation cycles, and the current density was then increased to 1 mA cm^{-2} for all the following cycles. The voltage evolution during the testes is shown in Figure 3d. The cell based on FE showed dramatic voltage fluctuations when it was subjected to 1 mA cm^{-2}, which implies inhomogeneous lithium stripping/plating. Since its voltage reached the cutoff limit of 0.3 V, the cell was terminated at the 10th cycle (around 55 h). This phenomenon was not observed in the Li/FE/Cu cell subjected to even higher current densities (Figure 3c), which implies the negative effect of pristine LMAs' native SEI on the lithium stripping/plating.[41,42] With respect to the Li/Li cell, the Li/Cu cell employed Cu foil as the working electrode. In the formation cycle, this latter cell was subjected to a much larger plating/stripping capacity, enabling the effective reconstruction of the native SEI into an electrolyte-derived SEI. Therefore, the Li/Cu cell was less affected by the native SEI with respect to the Li/Li cell. It is also noticed that the dramatic voltage fluctuations were not observed for Li/Li cells when the LCILEs were employed (Figure 3d), which can be attributed to their superior Li^+ transport properties, weakening the effect of the native SEI on the LMAs. Therefore, the voltage fluctuation and short life span of Li/FE/Li cell can be attributed to the inhomogeneous lithium stripping/plating because of pristine LMAs' native SEI and sluggish Li^+ transport in FE. For the cell based on FECF, the polarization continuously increased upon cycling until a short circuit occurred at the 170th cycle (376 h).

By contrast, the cells employing either FEF or FEOCF showed stable long-term cycling up to 500 cycles, proving the promoted interfacial compatibility of LMAs toward the electrolytes with BnF and BnOCF as the cosolvents. Additionally, the voltage evolution of these two cells was different. For the FEOCF-based cell, the polarization was rather stable from the 50th to the 400th cycle, i.e., 136–836 h, but it quickly increased from 52 mV at the 400th cycle to 75 mV at the 500th cycle (1036 h), which indicates a rapid interfacial degradation in the last 100 cycles. Despite a higher polarization, the cell based on FEF did not show this phenomenon, implying that FEF exhibits a better interfacial compatibility with LMAs than FECF. The voltage profiles at selected cycles are shown in Figure S9 (Supporting Information).

2.3. Electrochemical Performance of NCA Cathodes

The anodic stability of the electrolytes was evaluated via linear sweep voltammograms using carbon-black-coated Al foils as working electrodes with a scan rate of 0.1 mV s^{-1}. As shown in Figure S10 (Supporting Information), the addition of the cosolvents led to decreased anodic stability, but the anodic current density at 4.4 V versus Li/Li^+ was lower than 2 μA cm^{-2} for all the electrolytes, suggesting their possible use for the 4 V class Ni-rich cathodes.

To study the compatibility of the electrolytes with Ni-rich cathode materials, Li/NCA coin cells with thick LMAs (500 μm, ≈103 mAh cm^{-2}), medium loading NCA cathodes (10 mg cm^{-2}), and large amount of electrolyte (75 μL for each cell) were assembled and tested at 20 °C in a voltage window of 2.8–4.4 V. After two formation cycles at 0.1C (1C is 200 mA g^{-1}, corresponding to a current density of 2 mA cm^{-2}), the cells were cycled at C/3 charge and 1C discharge. The evolution of discharge specific capacities and CEs during the tests are summarized in **Figure 4**a. The dis-/charge profiles of a few selected cycles for the FEOCF-based cell and the others are displayed in Figure 4b and Figure S11 (Supporting Information), respectively. The capacity of the cell with

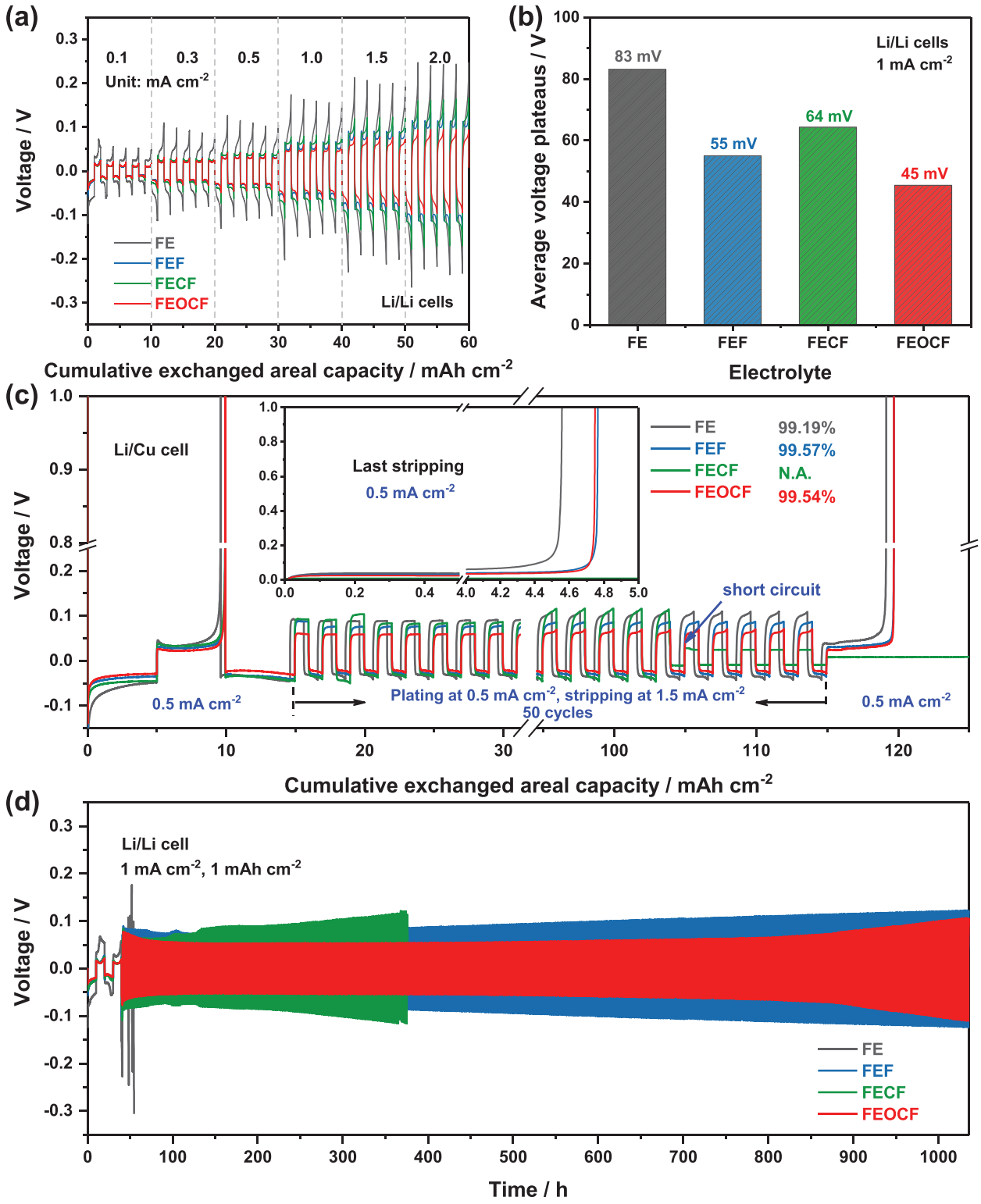

Figure 3. Electrochemical performance of LMAs in the electrolytes. a) Voltage profiles upon Li stripping/plating processes in Li/Li cells at various current densities. b) Average voltage plateaus of Li/Li cells operating at 1 mA cm^{-2} for 1 h. c) Voltage profiles of Li/Cu cells for the evaluation of Li plating/stripping CE in different electrolytes. The inset shows the voltage profile of the last stripping process. d) Voltage profiles of Li/Li cells upon long-term galvanostatic stripping/plating cycling.

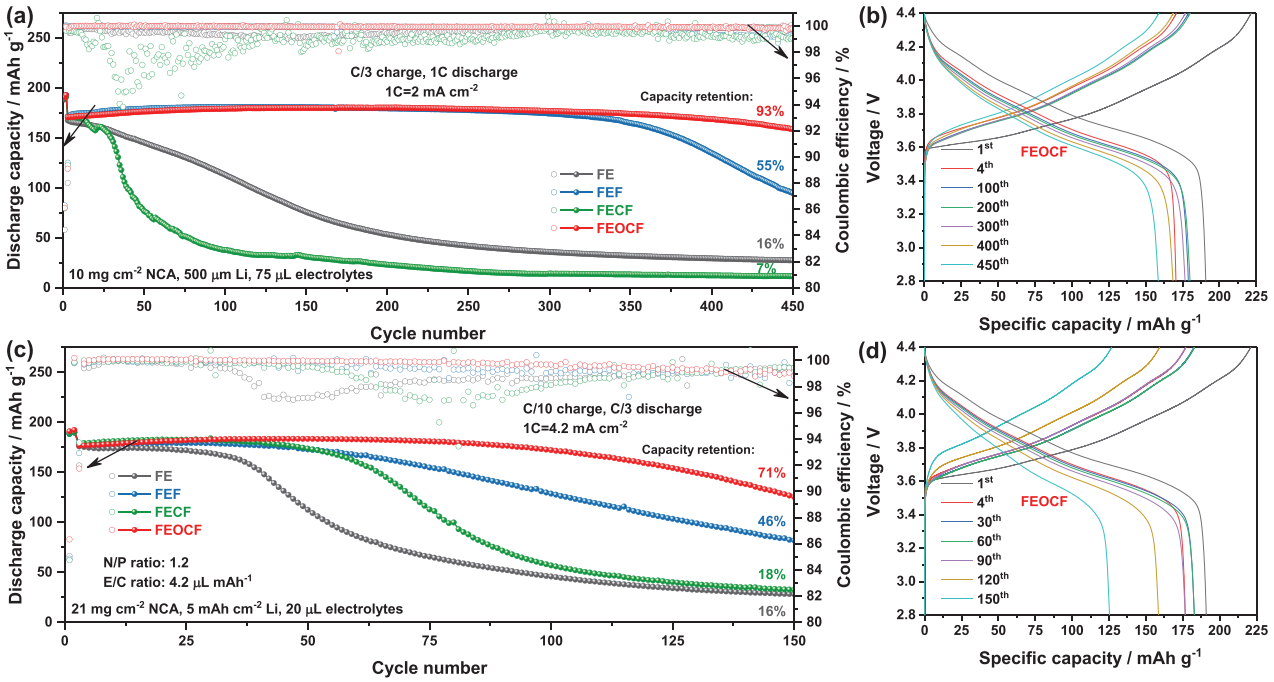

Figure 4. a,b) Electrochemical performance of Li/NCA cells with thick LMAs (500 μm), medium loading NCA cathodes (10 mg cm^{-2}), and excess electrolyte (75 μL): (a) evolution of discharge capacity and CE upon cycling at C/3 charge and 1C discharge after three formation cycles at C/10, (b) dis-/charge profiles of the Li/FEOCF/NCA cells at selected cycles. c,d) Electrochemical performance of Li/NCA cells with 5 mA cm^{-2} LMAs, high loading NCA cathodes (21 mg cm^{-2}), and relatively lean electrolyte (20 μL, 4.2 μL mAh^{-1}): (c) evolution of discharge capacity and CE upon cycling at C/10 charge and C/3 discharge after three formation cycles at C/10, (d) dis-/charge profiles of Li/FEOCF/NCA cells at selected cycles. In both cases, 1C corresponds to 200 mA g^{-1}.

FE decreased rapidly from 165 mAh g^{-1} at the 10th cycle to 76 mAh g^{-1} at the 150th cycle, which was accompanied by a decline of the CE from 99.77% to 99.12% and an increased cell polarization, as shown in Figure S12 (Supporting Information). When FECF was employed, the fading of the capacity and CE was even worse, which decreased from 170 mAh g^{-1} and 99.50% at the 10th cycle to 76 mAh g^{-1} and 96.22% at the 50th cycle. Since LMAs and electrolytes were used in significant excess, the observed decline of the capacity and CE in the early cycling originates from the cathode, indicating a poor and continuously worsening cathode/electrolyte interface in these two electrolytes. Taking together, one can further infer that the side reaction at the electrolyte/NCA interface due to their limited compatibility leads to the increased cell polarization and, consequently, the capacity fading. At the 450th cycle, the cells employing FE and FECF retained only 16% and 7% of the capacity achieved at the 4th cycle.

On the contrary to BnCF, the addition of BnF and BnOCF to FE resulted in higher and more stable CEs, as well as improved cyclability. The capacity retention was 93% and 55% under the same test conditions for FEOCF and FEF, respectively. In the 4th–300th cycles, the average CEs of cells employing FEF and FEOCF were 99.92% and 99.94%, respectively, and both cells exhibited negligible capacity fading. These findings demonstrate reinforced interfacial compatibility between these two electrolytes and NCA cathodes. In the subsequent 150 cycles, the FEF-based cell experienced a capacity decrease from 174 to 95 mAh g^{-1} and a reduced average CE of 99.55%, while the FEOCF-based cell showed only a slight capacity fading from 178 to 159 mAh g^{-1} and a much higher average CE of 99.89%. The capacity fading during such long-term tests (around 10 weeks) is usually caused by the degradation of the interfaces at both anodes and cathodes.[40] Nonetheless, it was demonstrated in the last section that the LMA/electrolyte interface was more stable in FEF than in FEOCF (Figure 3c,d). In fact, the Li/FEF/NCA cell already exhibited a higher polarization than the Li/FEOCF/NCA cell at the 200th cycle (around 750 h), as shown in Figure S12 (Supporting Information), while Li/FEF/Li and Li/FEOCF/Li cells were both stable at a similar operation duration (Figure 3d). Therefore, the superior cyclability of Li/NCA cells using FEOCF can be attributed to a more robust cathode/electrolyte interface in FEOCF than in FEF. Additionally, electrochemical impedance spectroscopy measurements of Li/Li and Li/NCA cells employing FEOCF demonstrate that the kinetics of Li/FEOCF/NCA cell is mainly controlled by the NCA cathode side (Figure S13, Supporting Information). The capacity loss of Li/FEOCF/NCA cells fully charged to 4.4 V at C/3 and C/10 upon 120 h storage at open circuit was, respectively, only 2.0% and 1.5% (Figure S14, Supporting Information). Moreover, the Nyquist plots of Li/FEOCF/NCA cell after 2 and 182 cycles show a neglectable change of the high-frequency intercepts (Figure S15, Supporting Information), implying that there is not significant degradation of the electrolyte upon cycling. These results reveal the high stability of EEIs generated in the Li/FEOCF/NCA cells. The rate capability of the Li/FEOCF/NCA cell was also evaluated at 20 and 40 °C, as summarized in Figure S16 (Supporting Information). Due to the reduced viscosity and promoted ionic conductivity of the electrolyte at 40 °C,

the cell operating at the highest temperature delivered the highest specific capacity under the same current rate.

In a further step, coin cells with high loading NCA cathodes (21 mg cm^{-2}), thin LMAs (5 mAh cm^{-2}), and relatively lean electrolyte usage of 20 µL for each cell were assembled, exhibiting a N/P ratio of 1.2 and an E/C ratio of 4.2 µL mAh^{-1}. The LMAs were prepared via predeposition of lithium on Cu foil with Li/Cu cells, and their morphology was characterized via scanning electronic microscopy (SEM), as shown in Figure S17 (Supporting Information). These Li/NCA cells were still tested at 20 °C in the voltage window of 2.8–4.4 V. After two formation cycles at 0.1C (1C is 200 mA g^{-1}, i.e., 4.2 mA cm^{-2}), the cells were charged at C/10 and discharged at C/3 for the following cycles. The evolution of the capacity and CE is displayed in Figure 4c. Furthermore, dis-/charge profiles of cells with FEOCF and the other electrolytes at selected cycles are shown in Figure 4d and Figure S18 (Supporting Information), respectively. Compared to the previous run (Figure 4a,b), the cells employing FE and, especially, FECF showed better cycling stability in the first 30 cycles under the harsh conditions, which can be attributed to the use of lower current densities and specific currents weakening the effect of cathode passivation on the cell polarization. Such an effect is more pronounced for FECF than for FE, leading to better cyclability of the cell employing FECF with respect to the one employing FE (Figure 4c). Nonetheless, rapid capacity fading was observed again in the following cycles under these lean conditions, leading to a low capacity retention of 16% for FE and 18% for FECF after 150 cycles. Since the increased NCA mass loading accelerated the interfacial side reactions, the Li/FEF/NCA cell showed under these conditions lower discharge capacity and faster capacity fading than the Li/FEOCF/NCA cell already from the 50th cycle. At the 150th cycle, the delivered discharge specific capacity was 99 mAh g^{-1} for FEF and 125 mAh g^{-1} for FEOCF, which corresponded to capacity retentions of 46% and 71%, respectively. Therefore, the comparable interfacial stability at the LMA side and more robust interfacial compatibility with NCA cathode of FEOCF with respect to that of FEF lead to the significantly promoted cyclability of Li/NCA cells under lean conditions close to the practical application. Based on the weight of anode and cathode active materials, the specific energy and specific power realized with FEOCF were calculated to be 662 Wh kg^{-1} and 69 W kg^{-1} at 0.1C, and 620 Wh kg^{-1} and 225 W kg^{-1} at the elevated current rate (Figure S19, Supporting Information). Table S4 (Supporting Information) compares the lithium stripping/plating CEs and performance of 4 V class LMBs employing the reported ILEs, LCILEs, and a few electrolytes recently reported in the literature. The electrolyte developed in this work exhibits high reversibility of LMAs and cyclability of LMBs, particularly considering the low N/P ratio and high areal capacity of cathodes.

2.4. Chemistry at Electrode/Electrolyte Interphases

The electrochemical performance clearly demonstrates the significant influence of the different cosolvents on the interfacial compatibility of the electrolytes with LMAs and NCA cathodes. To understand this influence, the electrodes of Li/NCA cells employing 500 µm thick LMAs, 10 mg cm^{-2} NCA cathodes, and 75 µL electrolyte for each cell were unmounted and characterized after cycling for 50 cycles.

Figure 5a–d exhibits the surface morphology of the LMAs observed with SEM. Dendritic lithium was not observed in any of the samples, but the electrodes became porous upon repeated lithium stripping/plating. The FE- and, particularly, FECF-based samples exhibited large hollows and long cracks with dimensions of more than 10 µm and were much more porous than the FEF and FEOCF-based samples with pores smaller than 2 µm. The higher porosity means more contact surfaces between the LMAs and electrolytes, which can accelerate their interfacial side reactions. The degradation extent of the LMAs was more obviously visualized by the cross-sectional SEM images shown in Figure 5e–h. On top of the LMAs, porous corrosion layers were observed. Their thicknesses were measured to be 67, 27, 106, and 25 µm for the LMAs cycled in FE, FEF, FECF, and FEOCF, respectively. Therefore, the addition of BnCF as a cosolvent to FE was detrimental for the cycling stability of LMAs, while that of BnF and BnOCF was helpful. These results match well with the presented electrochemical performance of LMAs in these electrolytes.

The cycled LMAs were further characterized with X-ray photoelectron spectroscopy (XPS) to investigate the influence of the different cosolvents on the composition of the SEI layers generated in the electrolytes. The photoelectron spectra were calibrated using the main C 1s peak (C—C/C—H at 284.8 eV) as reference, and more details of the C 1s spectra can be found in Figure S20 (Supporting Information). The spectra in the F 1s, N 1s, and S 2p region are shown in Figure 5i. For the SEI generated in FE, the peaks located at 685.0 and 688.0 eV in the F 1s spectrum can be assigned to S—F and LiF from the deposited and/or decomposed FSI^-.[43,44] The contribution of FSI^- to the SEI formation was also evidenced in the S 2p XPS spectrum, in which three peak doublets with S $2p_{3/2}$ peaks at 170.0, 168.6, and 166.8 eV were detected and can be attributed to the sulfur atom in FSI^- (S_{anion}), sulfate, and sulfite, respectively.[44,45] As FSI^- is the only source of sulfur in the electrolyte and the cell, the presence of these species proves the contribution of FSI^- to the SEI. In the N 1s spectrum, the peaks located at 401.7 and 399.6 eV represent the positively charged nitrogen atoms (N_{cation}) from $Emim^+$ and negatively charged nitrogen atoms (N_{anion}) from FSI^-, respectively, while the peak at 398.4 eV (N_{dec}) can be attributed to nitrogen-containing species derived from the decomposition of $Emim^+$ and FSI^-.[43,46,47]

The components making up the SEIs generated in LCILEs were very similar to that in the neat ILE (FE). Interestingly, the cosolvents BnF, BnCF, and BnOCF were not inserted into the SEI layer in a measurable extent. In fact, the F 1s peak of the fluorine atoms in these compounds, which is expected to appear at 689–691 eV,[48,49] could not be detected in all three cases. Despite the similar components, their concentration was affected by the use of the different cosolvents. When BnCF was used as the diluent, the signals associated with FSI^- got significantly enhanced, viz., S—F (F 1s), N_{anion} (N 1s), and S_{anion} (S 2p), demonstrating increased deposition and/or decomposition of FSI^-. A similarly enhanced contribution of FSI^- to the SEI was also observed for FEF. In addition, the SEI of the sample cycled in this electrolyte exhibited an increased contribution of $Emim^+$, as proved by the higher intensity of N_{cation} (N 1s). The previous electrochemical results

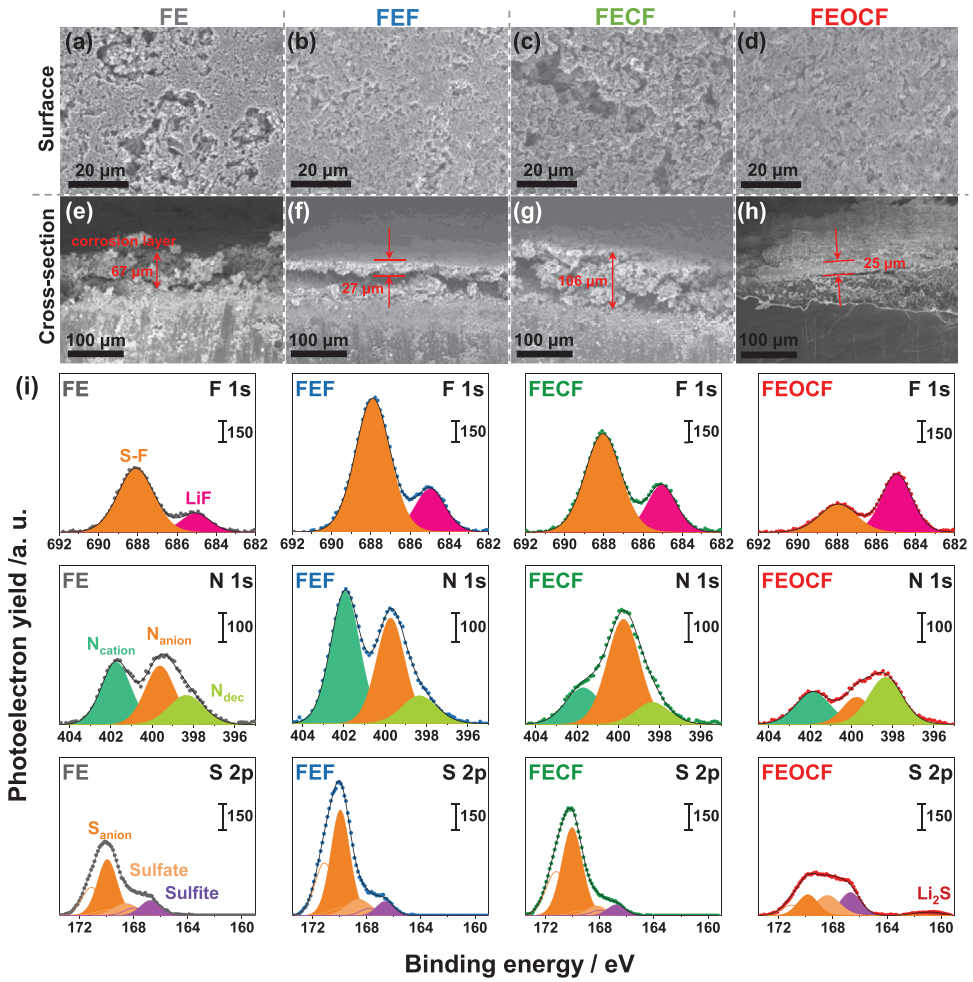

Figure 5. Characterization of LMAs unmounted from Li/NCA cells after 50 cycles. SEM images of LMAs cycled in a,e) FE, b,f) FEF, c,g) FECF, and d,h) FEOCF. i) XPS detail spectra in the F 1s, N 1s, and S 2p regions for the cycled LMAs (after background subtraction).

demonstrated that BnF as cosolvent promoted the reversibility of LMAs, while BnCF led to a worse reversibility of LMAs. Therefore, these results reveal the beneficial effect of $Emim^+$-derived species and the negative effect of the deposition and/or incomplete decomposition of FSI^- on the stability of SEIs. Finally, compared with the FE-based sample, the spectra of the sample tested in FEOCF showed decreased intensity of the features of both $Emim^+$ (N_{cation} (N 1s)) and FSI^- (S—F (F 1s), N_{anion} (N 1s), and S_{anion} (S 2p)), which was accompanied by increased intensity of LiF (F 1s) and N_{dec} (N 1s). Moreover, the presence of BnOCF cosolvent led also to the formation of Li_2S (peak doublet with S $2p_{3/2}$ component at 160.6 eV).[44] As previously demonstrated, these inorganic species, particularly LiF, with high interfacial energy with lithium metal and high mechanical strength are desired interphase components suppressing interfacial side reactions.[47,50] Therefore, the addition of FEOCF as a cosolvent promoted a more complete decomposition of FSI^- and/or $Emim^+$, leading to the promoted reversibility of LMAs. Via comparing the spectra collected from the LMAs cycled in FEF and FEOCF, it can be concluded that the SEI generated in FEOCF exhibited more inorganic components, which could be the reason for a lower polarization of LMAs in FEOCF than in FEF, as observed in Figure 3.

In the next step, the characterization of the cycled NCA cathodes was performed. SEM images from the surface of the electrodes in the pristine state and after cycling in the various electrolytes are shown in Figure S21 (Supporting Information) and **Figure 6**a–h, respectively. Secondary NCA microspheres consisting of well-defined sub-micrometer primary particles were observed for the pristine electrodes in Figure S21 (Supporting Information). After cycling in FE (Figure 6a,b) and FECF (Figure 6e,f), the surface of the particles was fully covered by a dense layer, i.e., a CEI, showing a texture apparently different from that of the pristine NCA particles. Additionally, some aggregates of bare carbon black nanospheres on the NCA were not covered by the layer, indicating that NCA is essential to the formation of the thicker CEI layer. Therefore, the coating layer observed after cycling can be attributed to the decomposition of electrolytes at the interface of NCA particles. By contrast, the well-defined NCA primary particles were still clearly observed for the electrodes cycled in FEF (Figure 6c,d) and FEOCF (Figure 6g,h), which indicates that the CEIs generated in FEF and FEOCF are much thinner than that in FE and FECF. The thicker CEIs in FE and FECF correlate well with the fast capacity fading of the Li/NCA cells employing these two electrolytes, resulting from the

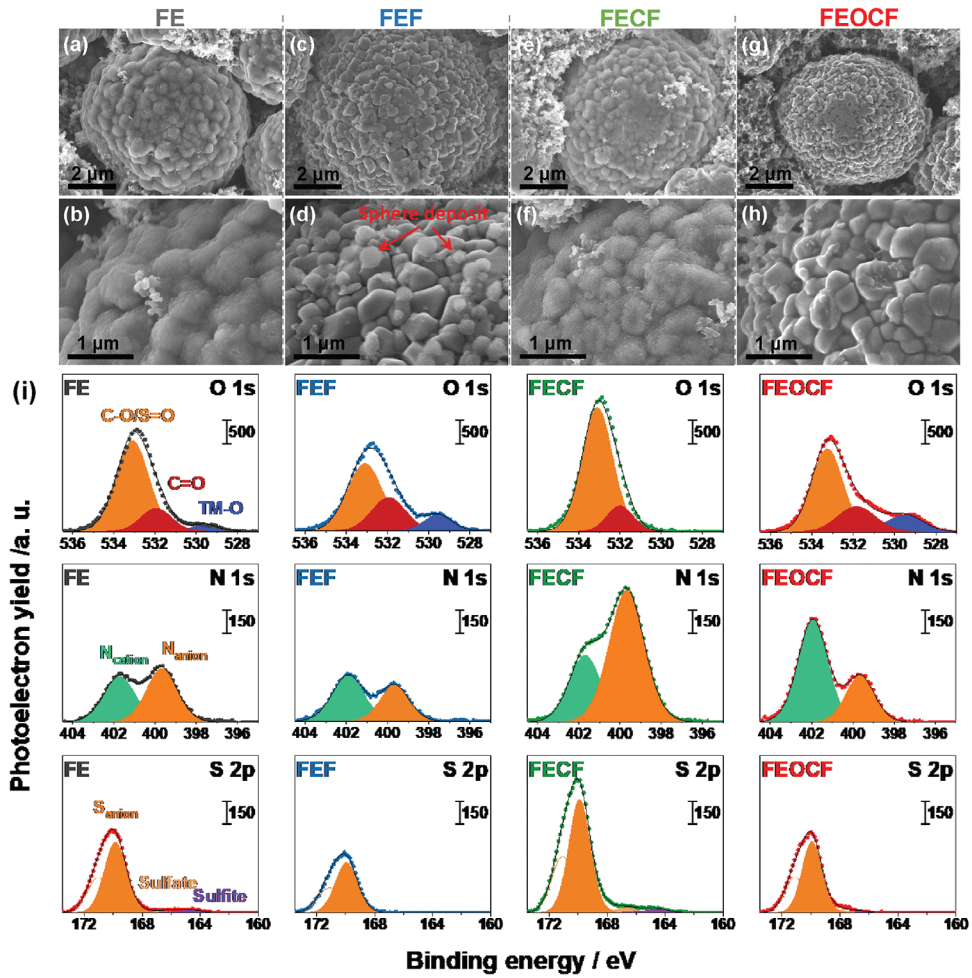

Figure 6. Characterization of NCA cathodes unmounted from Li/NCA cells after 50 cycles. SEM images of NCA electrodes cycled in a,b) FE and c,d) FEF, e,f) FECF, and g,h) FEOCF. i) XPS detail spectra in the O 1s, N 1s, and S 2p region for the cycled NCA cathodes (after background subtraction).

passivation of the electrodes. In the SEM images of the FEF-based sample (Figure 6c,d), some spherical deposits with a diameter of a few hundred nanometers and lighter contrast than NCA particles were observed, which can be ascribed to electrolyte decomposition upon cycling. But these spherical deposits were not observed for the electrode tested in FEOCF. This means that the CEI generated in FEOCF is more uniform than in FEF, preventing the undesired electrolyte decomposition and promoting the cyclability of NCA cathodes (Figure 4a,c).

Energy dispersive X-ray (EDX) spectroscopy was applied to analyze the elemental composition in a randomly selected region with a size of 85 × 110 μm on the surface of the electrodes. The SEM images of the selected regions and the corresponding EDX spectra are shown in Figure S22 (Supporting Information). The obtained atomic elemental compositions are collected in Table S5 (Supporting Information). In general, the proportion of nickel was reduced and the portion of fluorine, sulfur, and nitrogen was increased after cycling, which is related to the formation of the electrolyte-derived CEIs. Considering the specific composition of the different samples, one can infer that the amount of CEI generated on the electrodes during the cycling follows the trend of FECF > FE > FEF > FEOCF, with the electrodes tested in FEF and FEOCF being very close, which perfectly match with the cycling test results reported in Figure 4a.

To reveal the chemical nature of the observed CEIs, the cycled NCA samples were also subjected to XPS measurements. The C 1s peak (C—C/C—H at 284.8 eV) was used as reference to calibrate the photoelectron spectra (Figure S23, Supporting Information). The O 1s, N 1s, and S 2p spectra of the cycled electrodes are shown in Figure 6i. In the O 1s region, three peaks located at 533.3, 531.8, and 529.5 eV were observed, which can be attributed to the oxygen atoms in C—O/S═O, C═O, and transition metal oxides (TM—O), respectively.[12,44,51] Particularly, the intensity of the TM—O peak reflects the thickness of the deposited CEIs. This peak was not observed for the electrode tested in FECF, indicating that the NCA electrode was fully covered by a CEI thicker than the detection depth of the XPS. Compared with the electrode tested in FE, the ones cycled in FEF and FEOCF exhibited more intense TM—O peaks, indicating thinner CEIs, i.e., reduced electrolyte decomposition, in the presence of BnF and BnOCF. The peak intensity was very similar for the electrodes cycled in FEF and FEOCF.

The species detected in the N 1s and S 2p XPS spectra collected on NCA cathodes were very similar to those observed on

LMAs. Compared with FE, FECF led to significantly increased peak intensities of S_{anion} (S 2p) and N_{anion} (N 1s), which indicates an increased contribution of FSI^- to the CEI formation in FECF. By contrast, the sample cycled in FEF exhibited lower intensity of these peaks, reflecting a reduced contribution of FSI^- to the CEI in the presence of BnF cosolvent. When BnOCF was added to FE as the cosolvent, the contribution of FSI^- to the CEI was not affected, as evidenced by the generally comparable intensity of S_{anion} (S 2p) as well as N_{anion} (N 1s) peak. However, the N_{cation} peak in the N 1s XPS spectra was much larger for the electrode cycled in FEOCF, demonstrating the promoted contribution of $Emim^+$ to the CEI in the presence of BnOCF. Correlating these findings with the surface morphology and the electrochemical performance, one can infer that the massive and uncontrollable decomposition of FSI^- on NCA cathodes is responsible for the rapid passivation of the active material resulting in the capacity fading in FE and FECF, while the promoted decomposition of $Emim^+$ on NCA cathodes in FEOCF leads to a more protective and stable CEI resulting to a better cyclability than FE and FEF.

The F 1s spectra of these electrodes were also fitted as shown in Figure S24 (Supporting Information). Nonetheless, the contribution of the polyvinylidene fluoride binder in the electrodes (peak at 688.0 eV) does not enable a meaningful analysis of the fluorine species in the CEI.

3. Conclusion

LCILEs with three different cosolvents, namely BnF, BnCF, and BnCOF were prepared and systematically compared with the neat ILE in terms of their physical properties, solution structure, electrochemical performance, as well as EEIs. The fluorinated groups tethered to the benzene ring of the cosolvents affected the ionic conductivity and viscosity of LCILEs through the π–π stacking between aromatic $Emim^+$ and cosolvents, as well as the coordination between Li^+ and the fluorine atoms of the cosolvents, which were governed by the charge density of the benzene ring and fluorine atom, respectively. Moreover, it was found that the different fluorinated groups of the benzene-based cosolvent affected the reversibility of LMAs and NCA cathodes in the LCILEs via adjusting the contribution of $Emim^+$- and/or FSI^--derived species to the EEIs. The massive deposition and/or incomplete decomposition of FSI^- negatively affected the interfacial stability of LMAs and NCA cathodes, while the species derived from $Emim^+$ were generally beneficiary to a more protectively EEIs on both electrodes. A LCILE employing BnOCF as cosolvent leading to a protective SEI on LMAs and, particularly, to a uniform CEI rich in $Emim^+$-derived species on NCA cathodes was proposed for use in practical LMBs.

Supporting Information

Supporting Information is available from the Wiley Online Library or from the author.

Acknowledgements

This work was supported by the China Scholarship Council; the Helmholtz Association Basic funding; the postdoctoral fellowship in the framework of the "MSCA EF Master Class 2018" funding programme in the Politecnico di Milano.

Open access funding enabled and organized by Projekt DEAL.

Conflict of Interest

The authors declare no conflict of interest.

Author Contributions

X.L.: conceptualization, electrochemical tests, writing-original draft. A.M.: MD and DFT simulations, writing-review and editing. T.D.: XPS measurements, writing-review and editing. M.E.D.P.: NMR measurements, writing-review and editing. X.D.: tests for physicochemical properties, writing-review and editing. A.M.: NMR measurements, writing-review and editing. S.P.: supervision, funding acquisition, writing-review and editing.

Data Availability Statement

The data that support the findings of this study are available on request from the corresponding author. The data are not publicly available due to privacy or ethical restrictions.

Keywords

electrode/electrolyte interphases, ionic liquids, lithium metal batteries, locally concentrated electrolytes, trifluoromethoxybenzene

Received: September 4, 2023
Revised: November 9, 2023
Published online:

[1] X. He, D. Bresser, S. Passerini, F. Baakes, U. Krewer, J. Lopez, C. T. Mallia, Y. Shao-Horn, I. Cekic-Laskovic, S. Wiemers-Meyer, F. A. Soto, V. Ponce, J. M. Seminario, P. B. Balbuena, H. Jia, W. Xu, Y. Xu, C. Wang, B. Horstmann, R. Amine, C.-C. Su, J. Shi, K. Amine, M. Winter, A. Latz, R. Kostecki, *Nat. Rev. Mater.* **2021**, *6*, 1036.
[2] W. Li, E. M. Erickson, A. Manthiram, *Nat. Energy* **2020**, *5*, 26.
[3] J.-G. Zhang, W. Xu, J. Xiao, X. Cao, J. Liu, *Chem. Rev.* **2020**, *120*, 13312.
[4] G.-L. Xu, X. Liu, A. Daali, R. Amine, Z. Chen, K. Amine, *Adv. Funct. Mater.* **2020**, *30*, 2004748.
[5] W. Xue, M. Huang, Y. Li, Y. G. Zhu, R. Gao, X. Xiao, W. Zhang, S. Li, G. Xu, Y. Yu, P. Li, J. Lopez, D. Yu, Y. Dong, W. Fan, Z. Shi, R. Xiong, C.-J. Sun, I. Hwang, W.-K. Lee, Y. Shao-Horn, J. A. Johnson, J. Li, *Nat. Energy* **2021**, *6*, 495.
[6] H. Wang, Z. Yu, X. Kong, S. C. Kim, D. T. Boyle, J. Qin, Z. Bao, Y. Cui, *Joule* **2022**, *6*, 588.
[7] S. Chen, C. Niu, H. Lee, Q. Li, L. Yu, W. Xu, J.-G. Zhang, E. J. Dufek, M. S. Whittingham, S. Meng, J. Xiao, J. Liu, *Joule* **2019**, *3*, 1094.
[8] M. Wu, Z. Wang, W. Zhang, C. Jayawardana, Y. Li, F. Chen, B. Nan, B. L. Lucht, C. Wang, *Angew. Chem., Int. Ed.* **2023**, *62*, e202216169.
[9] S. Zhang, X. Zhuang, X. Du, X. Zhang, J. Li, G. Xu, Z. Ren, Z. Cui, L. Huang, S. Wang, F. Sun, L. Qiao, S. Dong, G. Cui, *Adv. Mater.* **2023**, *35*, 2301312.
[10] S. Chen, J. Fan, Z. Cui, L. Tan, D. Ruan, X. Zhao, J. Jiang, S. Jiao, X. Ren, *Angew. Chem., Int. Ed.* **2023**, *62*, e202219310.
[11] Y. Zou, G. Liu, Y. Wang, Q. Li, Z. Ma, D. Yin, Y. Liang, Z. Cao, L. Cavallo, H. Kim, L. Wang, H. N. Alshareef, Y.-K. Sun, J. Ming, *Adv. Energy Mater.* **2023**, *13*, 2300443.

[12] F. Wu, S. Fang, M. Kuenzel, A. Mullaliu, J.-K. Kim, X. Gao, T. Diemant, G.-T. Kim, S. Passerini, *Joule* **2021**, *5*, 2177.
[13] U. Pal, D. Rakov, B. Lu, B. Sayahpour, F. Chen, B. Roy, D. R. Macfarlane, M. Armand, P. C. Howlett, Y. S. Meng, M. Forsyth, *Energy Environ. Sci.* **2022**, *15*, 1907.
[14] P. Liang, H. Sun, C.-L. Huang, G. Zhu, H.-C. Tai, J. Li, F. Wang, Y. Wang, C.-J. Huang, S.-K. Jiang, M.-C. Lin, Y.-Y. Li, B.-J. Hwang, C.-A. Wang, H. Dai, *Adv. Mater.* **2022**, *34*, 2207361.
[15] A. Heist, S. Hafner, S.-H. Lee, *J. Electrochem. Soc.* **2019**, *166*, A873.
[16] X. Liu, A. Mariani, H. Adenusi, S. Passerini, *Angew. Chem., Int. Ed.* **2023**, *62*, e202219318.
[17] Y. Cai, Q. Zhang, Y. Lu, Z. Hao, Y. Ni, J. Chen, *Angew. Chem., Int. Ed.* **2021**, *60*, 25973.
[18] F. Lundin, A. Idström, P. Falus, L. Evenäs, S. Xiong, A. Matic, *J. Phys. Chem. C* **2022**, *126*, 16262.
[19] S. Lee, K. Park, B. Koo, C. Park, M. Jang, H. Lee, H. Lee, *Adv. Funct. Mater.* **2020**, *30*, 2003132.
[20] Z. Wang, F. Zhang, Y. Sun, L. Zheng, Y. Shen, D. Fu, W. Li, A. Pan, L. Wang, J. Xu, J. Hu, X. Wu, *Adv. Energy Mater.* **2021**, *11*, 2003752.
[21] X. Liu, T. Diemant, A. Mariani, X. Dong, M. E. Di Pietro, A. Mele, S. Passerini, *Adv. Mater.* **2022**, *34*, 2207155.
[22] X. Liu, A. Mariani, M. Zarrabeitia, M. E. Di Pietro, X. Dong, G. A. Elia, A. Mele, S. Passerini, *Energy Storage Mater.* **2022**, *44*, 370.
[23] X. Liu, A. Mariani, T. Diemant, M. E. D. Pietro, X. Dong, M. Kuenzel, A. Mele, S. Passerini, *Adv. Energy Mater.* **2022**, *12*, 2200862.
[24] D.-J. Yoo, S. Yang, K. J. Kim, J. W. Choi, *Angew. Chem., Int. Ed.* **2020**, *59*, 14869.
[25] Z. Jiang, Z. Zeng, X. Liang, L. Yang, W. Hu, C. Zhang, Z. Han, J. Feng, J. Xie, *Adv. Funct. Mater.* **2021**, *31*, 2005991.
[26] H. Tu, L. Li, Z. Wang, J. Wang, H. Lin, M. Wang, C. Yan, M. Liu, *ACS Nano* **2022**, *16*, 16898.
[27] M. Liu, X. Li, B. Zhai, Z. Zeng, W. Hu, S. Lei, H. Zhang, S. Cheng, J. Xie, *Batteries Supercaps* **2022**, *5*, 202100407.
[28] H. Zhang, Z. Zeng, R. He, Y. Wu, W. Hu, S. Lei, M. Liu, S. Cheng, J. Xie, *Energy Storage Mater.* **2022**, *48*, 393.
[29] M. Qin, Z. Zeng, X. Liu, Y. Wu, R. He, W. Zhong, S. Cheng, J. Xie, *Adv. Sci.* **2023**, *10*, 2206648.
[30] C. Zhu, C. Sun, R. Li, S. Weng, L. Fan, X. Wang, L. Chen, M. Noked, X. Fan, *ACS Energy Lett.* **2022**, *7*, 1338.
[31] M. Kunze, S. Jeong, E. Paillard, M. Schönhoff, M. Winter, S. Passerini, *Adv. Energy Mater.* **2011**, *1*, 274.
[32] A. Groß, S. Sakong, *Curr. Opin. Electrochem.* **2019**, *14*, 1.
[33] Y. Yang, H. Hua, Z. Lv, M. Zhang, C. Liu, Z. Wen, H. Xie, W. He, J. Zhao, C. C. Li, *Adv. Funct. Mater.* **2023**, *33*, 2212446.
[34] D. Wu, Y. Kang, F. Wang, J. Yang, Y. Xu, Y. Zhuang, J. Wu, J. Zeng, Y. Yang, J. Zhao, *Adv. Energy Mater.* **2023**, *13*, 2301145.
[35] M. Beran, J. Příhoda, Z. Žák, M. Cerník, *Polyhedron* **2006**, *25*, 1292.
[36] J. Wang, Y. Yamada, K. Sodeyama, C. H. Chiang, Y. Tateyama, A. Yamada, *Nat. Commun.* **2016**, *7*, 12032.
[37] W. Wahyudi, X. Guo, V. Ladelta, L. Tsetseris, M. I. Nugraha, Y. Lin, V. Tung, N. Hadjichristidis, Q. Li, K. Xu, J. Ming, T. D. Anthopoulos, *Adv. Sci.* **2022**, *9*, 2202405.
[38] Y. Wang, Z. Cao, Z. Ma, G. Liu, H. Cheng, Y. Zou, L. Cavallo, Q. Li, J. Ming, *ACS Energy Lett.* **2023**, *8*, 1477.
[39] B. Ganbold, G. Zheng, S. A. Willis, G. R. Dennis, W. S. Price, *J. Mol. Liq.* **2015**, *201*, 96.
[40] B. D. Adams, J. Zheng, X. Ren, W. Xu, J.-G. Zhang, *Adv. Energy Mater.* **2018**, *8*, 1702097.
[41] A. Etxebarria, S. L. Koch, O. Bondarchuk, S. Passerini, G. Teobaldi, M. Á. Muñoz-Márquez, *Adv. Energy Mater.* **2020**, *10*, 2000520.
[42] M. Baek, J. Kim, K. Jeong, S. Yang, H. Kim, J. Lee, M. Kim, K. J. Kim, J. W. Choi, *Nat. Commun.* **2023**, *14*, 1296.
[43] M. Olschewski, R. Gustus, M. Marschewski, O. Höfft, F. Endres, *Phys. Chem. Chem. Phys.* **2014**, *16*, 25969.
[44] J. F. Moulder, W. F. Stickle, P. E. Sobol, K. D. Bomben, *Handbook of X-Ray Photoelectron Spectroscopy*, Perkin-Elmer Corporation, Physical Electronics Division, MN, USA **1992**.
[45] C.-J. Huang, K.-Y. Lin, Y.-C. Hsieh, W.-N. Su, C.-H. Wang, G. Brunklaus, M. Winter, J.-C. Jiang, B. J. Hwang, *ACS Appl. Mater. Interfaces* **2021**, *13*, 14230.
[46] M. Olschewski, R. Gustus, O. Höfft, A. Lahiri, F. Endres, *J. Phys. Chem. C* **2017**, *121*, 2675.
[47] S. Liu, X. Ji, N. Piao, J. Chen, N. Eidson, J. Xu, P. Wang, L. Chen, J. Zhang, T. Deng, S. Hou, T. Jin, H. Wan, J. Li, J. Tu, C. Wang, *Angew. Chem., Int. Ed.* **2021**, *60*, 3661.
[48] D. T. Clark, D. Kilcast, D. B. Adams, W. K. R. Musgrave, *J. Electron Spectrosc. Relat. Phenom.* **1972**, *1*, 227.
[49] D. T. Clark, D. Kilcast, W. K. R. Musgrave, *J. Chem. Soc. D* **1971**, 516b.
[50] J. Chen, Q. Li, T. P. Pollard, X. Fan, O. Borodin, C. Wang, *Mater. Today* **2020**, *39*, 118.
[51] T. Chen, X. Li, H. Wang, X. Yan, L. Wang, B. Deng, W. Ge, M. Qu, *J. Power Sources* **2018**, *374*, 1.